Received: 29 June 2023 | Revised: 19 August 2023 | Accepted: 19 September 2023

DOI: 10.1002/jbio.202300252

RESEARCH ARTICLE

JOURNAL OF BIOPHOTONICS

Wide-field Mueller matrix polarimetry for spectral characterization of basic biological tissues: Muscle, fat, connective tissue, and skin

Iago Pardo | **Subiao Bian** | **Jordi Gomis-Brescó** | **Esther Pascual** | **Adolf Canillas** | **Salvador Bosch** | **Oriol Arteaga**

Dep. Fisica Aplicada, PLAT group, Universitat de Barcelona, Barcelona, Spain

Correspondence
Oriol Arteaga, Dep. Fisica Aplicada, PLAT group, Universitat de Barcelona, IN2UB Barcelona 08028, Spain.
Email: oarteaga@ub.edu

Funding information
Ministerio de Ciencia Innovación y Universidades, Grant/Award Numbers: PDC2022-133625-I00, TED2021-129639B-I00, RYC2018-024997-I, PID2022-138699OB-I00

Abstract

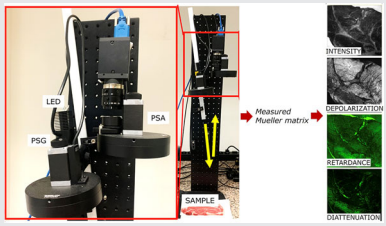

This study investigates the polarimetric properties of skin, skeletal muscle, connective tissue, and fat using Mueller matrix imaging. It aims to compare the polarimetric characteristics of these tissues and explore how they evolve with wavelength. Additionally, the temporal evolution of certain tissues during meat aging is studied, providing insights into the dynamic behavior of polarimetric properties over time. The research employs back-scattering configuration and the differential decomposition analysis method of Mueller matrix images. Both in-vivo and ex-vivo experiments were conducted using a consistent instrument setup to ensure reliable analysis. The results reveal wavelength-dependent variations in tissue properties, including an increase in depolarization with wavelength. Significant differences in the polarimetric characteristics of meat tissues, particularly for skeletal muscle, are observed. Over a 24-h period, intensity, diattenuation, and retardation experience alterations, being the decreased retardation in skeletal muscle and the increased retardation in fat the most notable ones.

KEYWORDS
Mueller matrix, polarimetry, polarization, tissue, turbid medium

1 | INTRODUCTION

Mueller matrix (MM) imaging is a versatile technique capable of providing spatially resolved measurements of polarization-dependent properties in materials and biological systems. It represents the most comprehensive experimental polarimetry study of linear interactions between light and matter. The real 4 × 4 Mueller matrix is an operator that contains complete information about the polarization and depolarization properties of the scattering medium. It enables quantitative evaluation of the measurements.

In the biomedical field, MM imaging has demonstrated its potential for various applications due to its sensitivity to microstructural tissue changes that affect light polarization. Despite being pioneered decades ago [1, 2],

MM imaging has recently gained popularity as a technique well-suited for biological and biomedical applications. It offers advantages such as harmlessness, noninvasiveness, good resolution, reduced cost and suitability for studying highly scattering media like biological tissues [3–17].

This article aims to provide an in-depth study of MM imaging in four fundamental biological tissues: skin (in-vivo), skeletal muscle, connective tissue and fat (all ex-vivo). We explore the evolution of the polarimetric properties of these tissues with respect to wavelength and also, with respect to time (for the ex-vivo tissues). We point out the challenges associated with their measurement, particularly the need to detect and measure small signals. The presented results are obtained using the same instrument for both in-vivo and ex-vivo experiments. By employing our standardized approach, we ensure a reliable and comparable analysis across different types of tissues. Skin, skeletal muscle, connective tissue and fat play crucial roles in biomedical research as they are key components of the human body and are involved in various physiological processes and pathological conditions. Hence, we expect that this comparative study will be useful in future investigations in this field, as it provides quantitative insights into the essential polarimetric properties of basic biological tissues.

2 | MATERIALS AND METHODS

2.1 | Instrument

Our instrument (Figure 1) utilizes a backscattering configuration, where light is reflected from the sample at a very small angle of incidence, around 10°. This configuration with an acute angle is advantageous for MM imaging since it eliminates the need for the beam-splitter used in systems where forward and backward light share the same optical path, simplifying the calibration process significantly. A backscattering configuration is well-suited for wide-field imaging systems, where the imaging optic elements are positioned at a considerable distance from the sample, enabling the examination of a wider sample area without compromising the measurements' quality. The imaging objective (a 16 mm fixed focal length camera objective Thorlabs MVL16M23) is positioned outside the region between the Polarizer-Sample-Analyzer components. By placing the objective away from this region, any potential polarization perturbation caused by strains or other factors can be minimized or avoided altogether. This ensures that the measured polarization properties of the sample remain unaffected and accurate. The camera used is FLIR Grasshopper3 (GS3-U3-32S4M-C) with a 12-bit ADC and a maximum resolution of 2448 × 2048 pixels (although the images reported in this work correspond to a region of interest of 600 × 600 pixels).

A Mueller matrix polarimeter consists of two essential components: a polarization-state generator (PSG) and a polarization-state analyzer (PSA). The PSG generates a minimum of four independent states of polarization that interact with the sample under investigation. On the other hand, the PSA analyzes the resulting states by measuring their projections onto at least four other linearly independent states.

In a Mueller matrix polarimetry experiment, the Stokes vector $\mathbf{S_{out}}$ reaching the detector is given by the equation [18]:

$$\mathbf{S_{out}} = \mathbf{M}_{\mathrm{PSA}}\mathbf{M}\mathbf{M}_{\mathrm{PSG}}\mathbf{S_{in}}, \tag{1}$$

where $\mathbf{M}$, $\mathbf{M}_{\mathrm{PSA}}$ and $\mathbf{M}_{\mathrm{PSG}}$ are respectively the Mueller matrices of the sample, the PSA and the PSG and $\mathbf{S_{in}}$ is the Stokes vector of the incident light coming from the light source. The analysis of polarimetric data involves the extraction of the Mueller matrix of the sample from the measured intensities. If the experiment consists of N intensity measurements ($k = 1,...,N$), the relationship can be expressed by the equation:

$$\mathbf{I} = \mathbf{W}\vec{\mathbf{M}}, \tag{2}$$

Here, $\mathbf{I} = (I_1, I_2, ..., I_N)^T$ represents the intensity vector across all measurements, and $\mathbf{W}$ is an $N \times 16$ matrix that relates the measured intensities to the elements of the 16-component Mueller vector $\vec{\mathbf{M}}$.

The elements of the Mueller matrix of the sample can be obtained by solving the equation [18]:

$$\vec{\mathbf{M}} = \left(\mathbf{W}^T\mathbf{W}\right)^{-1}\mathbf{W}^T\mathbf{I} = \mathbf{W}^{+}\mathbf{I}, \tag{3}$$

where $\mathbf{W}^{+} = \left(\mathbf{W}^T\mathbf{W}\right)^{-1}\mathbf{W}^T$ represents the pseudo-inverse of $\mathbf{W}$. The pseudo-inverse provides the least squares estimate of the inverse and is used when the number of measurements N is greater than 16. However, when $N = 16$, the pseudo-inverse coincides with the matrix inverse. In practice, the conditioning can often be improved by taking more than 16 measurements, thus over-specifying the calculations. However, the highest speed is typically achieved when utilizing $N = 16$, which is the configuration employed in this study.

In our system (Figure 1), the polarization-state generator (PSG) and polarization-state analyzer (PSA) are primarily composed of a compensator (Edmund Optics WP280 retarder) and a polarizer (Edmund Optics NIR polarizing film). However, we have implemented a

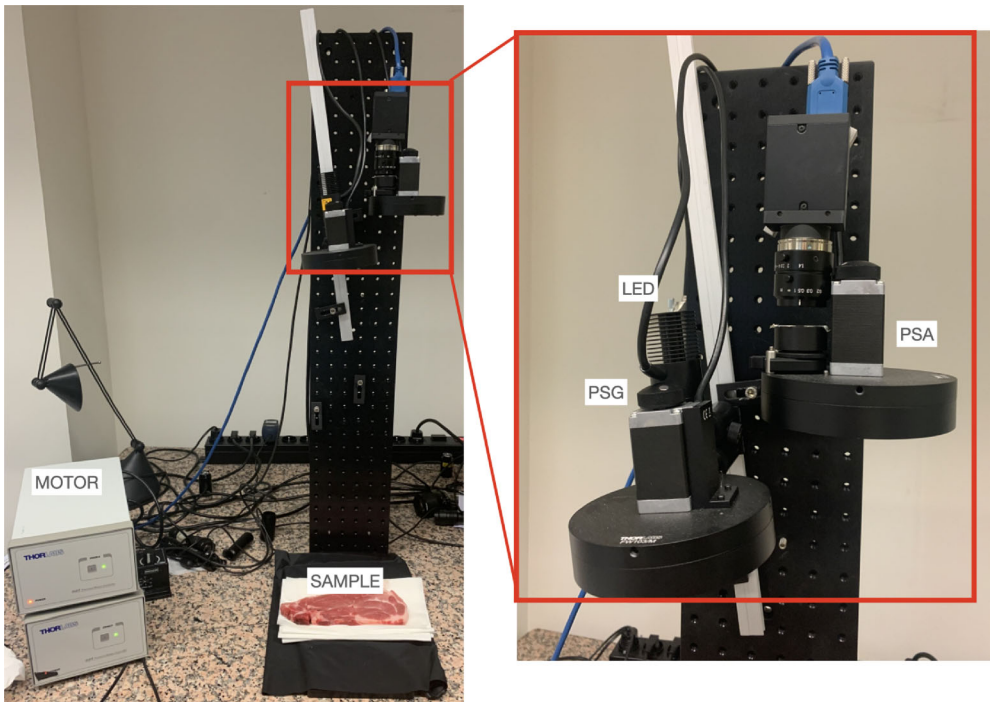

FIGURE 1 Wide-field imaging Mueller matrix polarimeter used in measurements. The different elements that make up the polarimeter are highlighted being the PSG and the PSA, the polarization state generator and the polarization state analyzer respectively.

unique design for the compensators in the PSG and PSA. We use four retarders in the PSG and four retarders in the PSA, which are mounted at pre-aligned orientations within fast-changing filter wheels (Thorlabs FW103H). These motorized fast-change filter wheels are specifically designed for applications that require sequential observations with different filters inserted into the optical path. The advantage of these filter wheels lies in their rapid switching time, approximately 55 ms, which significantly outperforms conventional rotating motors in terms of speed. The position of the filter wheel is controlled by a benchtop stepper motor, allowing precise control over the rotation. Each filter wheel contains six slots, in which we have fixed four retarders. This configuration enables the creation of 16 discrete angles of rotation by combining different retarders in different slots. Additionally, the filter wheels also feature two empty slots, providing flexibility for future modifications or alternate configurations using more states. By utilizing the motorized fast-change filter wheels, we achieve very quick and precise control over the orientations of the retarders in the PSG and PSA, so that a full MM image can be acquired in approximately 1.5 s. In the experiments detailed in this work, the overall measurement time for each MM measurement was around 10 seconds to ensure a certain degree of averaging on each acquired frame.

The polarizers in PSG and PSA were placed in a crossed configuration. The initial alignment of the retarders was conducted by setting them in the slots of the filter wheel to the theoretically optimal angles of $-15.1°$, $+15.1°$, $+51.7°$, and $-51.7°$, as established by Sabatke et al. [19]. This preliminary alignment was facilitated with the aid of a separate polarimeter from our laboratory [20]. However, the alignment was only approximate since given the delicate nature of these thin retarders, achieving precise orientation through manual manipulation is difficult; furthermore, there is also a noticeable wavelength-induced drift in the orientation fast axis of the retarders. Consequently, to ascertain the true values of orientation and retardance at varying wavelengths, a calibration procedure is necessary. This calibration process was executed employing a specularly reflecting mirror as a representative sample (which can be assumed to have MM $\mathrm{diag}(1,1,-1,-1)$) and using a nonlinear least square fitting algorithm that finds the retardance and orientation values to obtain a best fit to this matrix. Some calibration results are summarized in Table 1.

For imaging applications in the visible and near-infrared (NIR) ranges, the polymer film retarders we use offer several advantages over crystal-based retarders. Firstly, polymer film retarders are available in larger sizes, ensuring that the field of view of the instrument is not limited. Additionally, these film retarders are very thin, eliminating beam displacements that may occur upon rotation. Lastly, they are cost-effective, making them a practical choice.

The optimal retardance for the rotating compensator present in the PSG and PSA is approximately $\delta \sim 132°$ or $\sim 234°$, as deduced from studies on the determinant of $\mathbf{W}^{+}$ [19, 21]. By examining which retardance values yield the maximum determinant, these specific values are identified as the most suitable. However, commercially

TABLE 1 Calibration results of the offset angles and retardance.

Offset angles at 660 nm ±0.2 (deg)		Retardance ±0.1 (deg)
PSA	**PSG**	
0.1 (slot 0)	1.8 (slot 0)	254.5 (420 nm)
0.9 (slot 1)	1.5 (slot 1)	242.0 (455 nm)
0.1 (slot 2)	1.7 (slot 2)	145.7 (660 nm)
−0.5 (slot 3)	2.6 (slot 3)	121.6 (780 nm)

Note: All four retarders in PSG and PSA are assumed to have the same retardance that changes with wavelength. The offset angles refer to angle deviations of the fast axis from the reference values −15.1°, +15.1°, +51.7°, and −51.7°.

available film compensators are typically designed for non-optimal retardances of quarter wave ($\delta \sim 90°$) or half wave ($\delta \sim 180°$), resulting in reduced noise tolerance for the setup. Although these commercial film compensators are not fully achromatic, they exhibit close-to-optimal performance for a Mueller matrix ellipsometer at certain wavelengths outside of their design range. Notably, the half-wave polymer film compensator from Edmund Optics (WP280) used in this work offers two optimal regions: one between approximately 660 nm - 780 nm with a retardance of around 132°, and another around 420 nm - 480 nm where the retardance is close to 234° [22], as it is shown in Table 1. Thus, these compensators are particularly well-suited for imaging applications within these wavelength ranges, but cannot be used for Mueller matrix imaging in the green part of the spectrum. To achieve optimal film compensators for other wavelength ranges, one could effectively construct an elliptical retarder by combining two misaligned quarter-wave film retarders [21]. This approach allows for the customization of film compensators, enabling optimal performance in specific wavelength regions of interest [23].

2.2 | Samples

The experiments reported in this work correspond to two types of samples:

- In-vivo measurements were taken on the dorsum of the hand belonging to one of the authors (IP).
- Ex-vivo measurements were performed on porcine meat purchased from a local supermarket. The measurements were taken on fresh meat as well as aged meat for 24 h (stored at room temperature) and aged meat 96 h (stored at room temperature for the first 24 h and in a fridge for the remaining 72 h). All the meat results reported in this work correspond to measurements on the same slice of meat. However, repeated measurements on two additional meat samples exhibited consistent trends with the findings presented in this manuscript.

All measurements were conducted with the same instrument using back-scattering configuration, and no additional preparation of the samples was performed. These measurements provided results for four different types of tissues: human skin (obtained from the hand measurements), skeletal muscle, connective tissue, and fat (obtained from various parts of the porcine meat sample). For all samples, 4 different wavelengths (all of them close to the optimal range of our retarders) were measured: 420 nm, 450 nm, 660 nm, and 780 nm. Wavelengths were chosen by using different LED light sources with a bandpass of ∼10 nm.

Figure 2 shows an example of a Mueller matrix obtained for the porcine meat sample when measured at 780 nm. The imaged area is approximately 8.5 × 8.5 cm^2. The displayed image illustrates the typical characteristics of Mueller matrices observed in biological tissues: the off-diagonal elements are significantly small, multiplied by a factor of 10 in this figure to enhance visibility. Additionally, the diagonal elements also exhibit relatively modest values due to the extensive presence of multiple scattering within the tissue that randomizes the incoming polarization. These findings underscore the importance of employing instruments capable of detecting and accurately measuring subtle polarimetric signals when studying biological tissues.

2.3 | Analysis

Quantitative analysis of measured MM images is a key process to obtain images that show a good level of contrast that can be linked to physiological features of the tissues. In this work, we used the differential MM formalism to analyze the experimental data, as it is well adapted for biomedical polarimetric measurements since it is based on a continuously scattering medium model that is a good match for most biological tissues, and unlike certain serial decompositions does not depend on the order of constituent properties [24]. This method can decouple the individual contributions of several polarimetric effects occurring simultaneously [25–28].

In the context of depolarizing experimental Mueller matrices, the differential Mueller matrix **L** represents the local evolution of the Mueller matrix as light propagates through a homogeneous optical medium. To obtain **L**, one can compute the matrix logarithm of the experimental Mueller matrix **M**, denoted as $\mathbf{L} = \ln \mathbf{M}$. Numerical

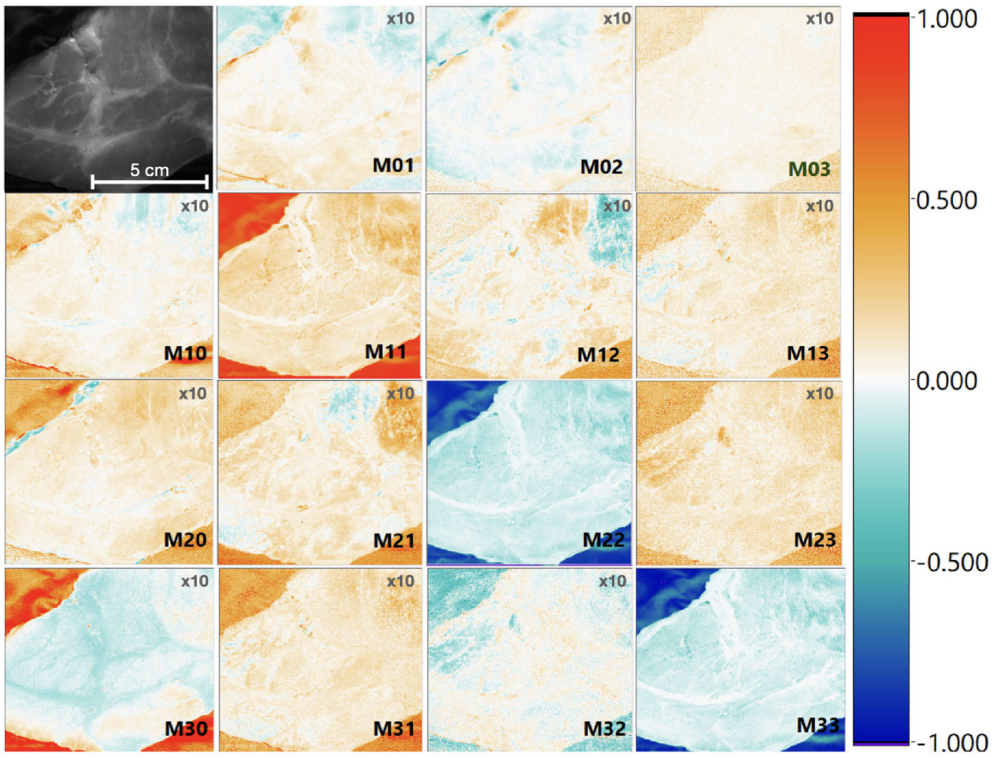

FIGURE 2 Example of normalized Mueller matrix measured for a pork meat sample using a 780 nm LED light source. M_{00} element has been replaced by the unpolarized intensity. All the off-diagonal elements have been multiplied by a factor of 10 to improve the visualization.

algorithms for calculating the matrix logarithm are readily available in modern programming software packages. For most depolarizing measurements in the backscattering configuration there exists no real matrix logarithm unless the sign of the last two rows is flipped by left-multiplying the experimental Mueller matrices measured in the backscattering configuration by the diagonal matrix $\mathrm{diag}(1,1,-1,-1)$ [29]. With this transformation of the measured matrix, the form of the matrix is made to resemble those measured in transmission, and the matrix logarithm can routinely be applied.

The polarization properties can be found from the elements of differential Mueller matrix **L** as:

- Horizontal linear retardance: $\mathrm{LR} = (l_{32} - l_{23})/2$,
- 45° linear retardance: $\mathrm{LR}' = (l_{13} - l_{31})/2$,
- Horizontal linear diattenuation: $\mathrm{LD} = (-l_{01} - l_{10})/2$,
- 45° linear diattenuation: $\mathrm{LD}' = (-l_{02} - l_{20})/2$

where l_{ij} indicate the elements of **L**. The magnitudes of linear retardance and linear diattenuation are then respectively calculated as $R_m = \sqrt{\mathrm{LR}^2 + \mathrm{LR}'^2}$ and $D_m = \sqrt{\mathrm{LD}^2 + \mathrm{LD}'^2}$. The values of the circular retardance and circular diattenuation can be also calculated from **L** but they have not been reported in this work as they were very small for all tissues and across all wavelengths.

As an additional metric to quantify the depolarization we use the depolarization index (DI) [30]

$$\mathrm{DI} = \sqrt{\frac{1}{3m_{00}^2}\left(\sum_{i,j=0}^{3} m_{ij}^2 - m_{00}^2\right)}, \tag{4}$$

which takes values between 1 (for a nondepolarizing MM) and 0 (for a fully depolarizing MM). Alternatively, the depolarization can be also quantified from the diagonal entries of the differential Mueller matrix **L**.

3 | RESULTS

3.1 | Comparison between tissues

The objective of our wide-field MM imaging results was to establish a quantitative comparison between different types of tissues when measured with the same instrument and experimental conditions. Such comparison was carried at different wavelengths, as it is illustrated in Figure 3 for the porcine meat sample. In this figure, some general trends can be already observed: depolarization increases with the increase of wavelength (DI becomes lower) because red and NIR light have longer penetration lengths in biological tissues, thus increasing the probability of polarization randomization due to multiple scattering. At the same time, this increase in the effective pathlength also produces a clear increase of retardation values at longer wavelengths.

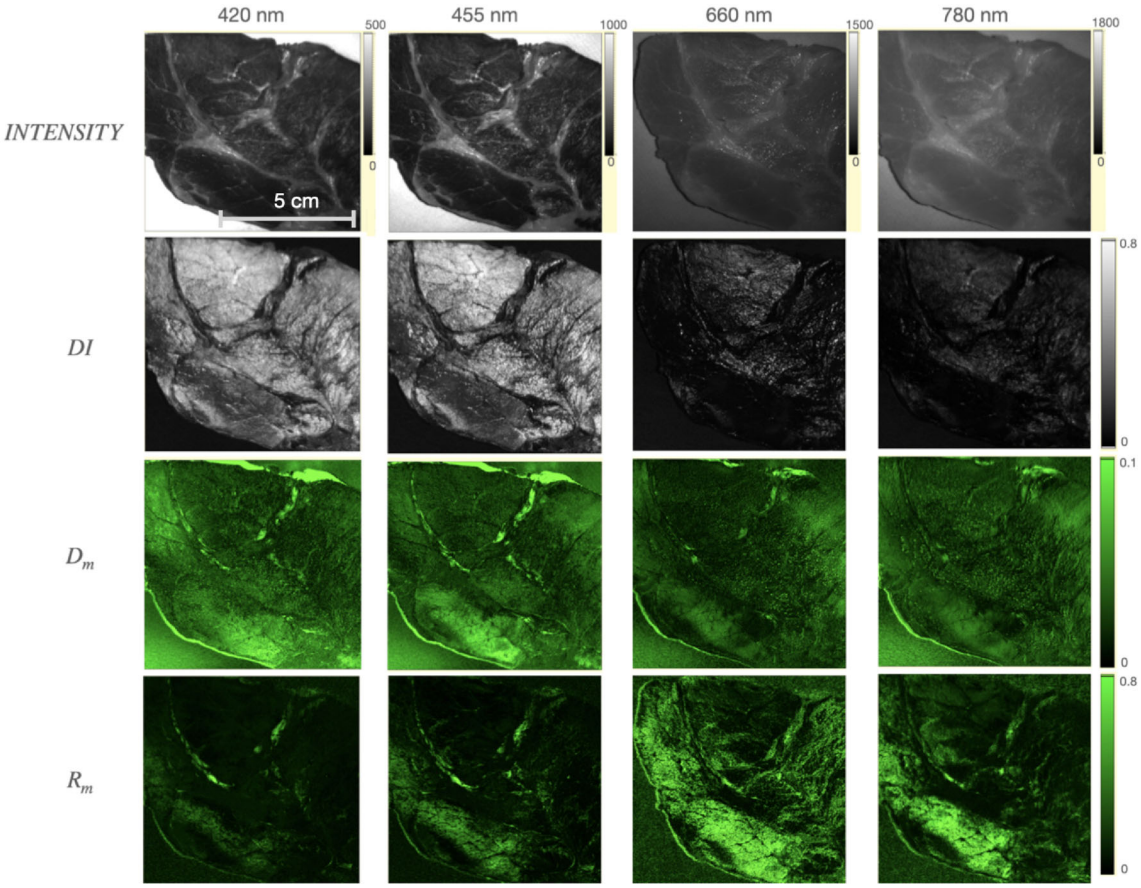

FIGURE 3 Comparison between measurements made in the same porcine sample at different wavelengths. We have measured various polarimetric properties such as the depolarization index (DI), diattenuation (D_m), and retardance (R_m).

The quantitative variation of DI, diattenuation (D_m) and retardance (R_m) as a function of wavelength are displayed in Figure 4 for the different tissues measured in the porcine meat sample and in human skin. The data points were obtained by sampling at least three different areas within the same sample for each different tissue. This approach was employed to ensure representative measurements and account for potential heterogeneity within the sample. Each tissue type was identified and targeted for measurements at specific locations within the sample as it is shown in Figure 4A. The error bars represent standard deviation of the parameters.

As shown in Figure 4, the DI demonstrates for all tissues a decreasing trend with increasing wavelength, with a relatively stable pattern observed in the reddish part of the spectrum (660 nm to 780 nm), except for fat, which shows a slight increase. This behavior can be attributed to the greater penetration depth of longer wavelengths, resulting in an extended photon path in the sample before reaching the detector. Consequently, more scattering events occur, leading to reduced polarization in the detected light. Additionally, the muscle exhibits notably higher DI values at shorter wavelengths compared to other tissues and experiences a more pronounced decrease as the wavelength increases. This observation can be attributed to the peak absorption band of myoglobin, a protein found in high concentrations in skeletal and cardiac muscle, occurring at around 550 nm, but also extending to the blue part of the electromagnetic spectrum. Thus, the presence of myoglobin leads to relatively large DI values in the blue, as absorption reduces the amount of multiple scattering, while at red or NIR wavelengths, the chromophores of the muscle do not absorb light significatively allowing for a large contribution from multiple scattering. Conversely, skin is comparatively slightly less depolarizing than other tissues in the red and NIR ranges.

From the diattenuation and retardation images of Figure 3, one can verify that the connective tissue generally shows higher values of these parameters than the other tissues. This fact can be attributed to the predominant composition of tendons within the connective tissue, which primarily consists of elastin and collagen fibers highly concentrated in specific orientations. Consequently, when exposed to light, the polarization of the light is substantially influenced by the alignment of the collagen fibers. Figures 3 and 4 also show a significant

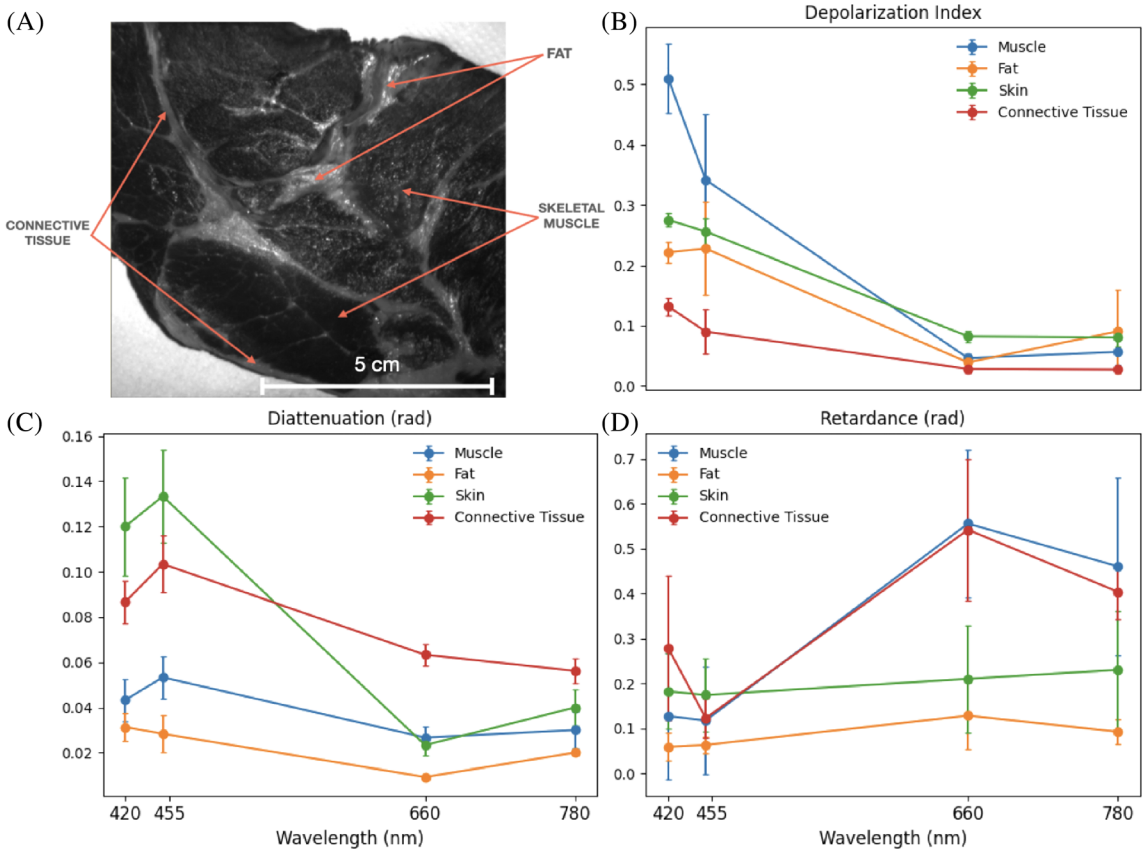

FIGURE 4 Identification of several tissues in the porcine meat sample (A). Variation of the depolarization index (B), diattenuation (C), and retardance (D) as a function of wavelength for different tissues in a pork meat sample and human skin.

increase in the retardance values observed at 660 nm and 780 nm in skeletal muscle and connective tissue. Again, this can be most likely attributed to the very low absorption of myoglobin at that wavelength, which leads to deep penetration of these longer wavelengths and increased pathlength. These factors contribute to increased scattering (low DI) and high retardation. On the other hand, the skin displays moderate levels of retardance, and its values remain relatively consistent across different wavelengths compared to the other tissues studied. Collagen, as the primary structural component of the dermis (the middle layer of the skin), plays a vital role in maintaining skin strength, elasticity, and overall structure. Collagen, like most birefringent materials, is expected to exhibit stronger retardance in the shorter-wavelength range, such as blue light. However, this effect is likely counterbalanced by the increased penetration of red and near-infrared light into the dermis layer. In all tissues, diattenuation values consistently remain lower than retardation values, with the blue spectral range generally exhibiting larger values compared to the red or NIR ranges, that are outside of the peak absorption bands of most biological chromophores.

In summary, among the measured tissues, muscle exhibits the lowest scattering (larger DI) in the blue part of the spectrum but one of the greatest multiple scattering responses in the red and NIR ranges. Connective tissue exhibits the strongest anisotropy, followed by muscle and skin, while fat generally displays the lowest anisotropy. This suggests that fat is mostly optically homogeneous, primarily depolarizing light without significant orientation-dependent polarization effects. However, it is worth noting that some anisotropy may be observed in fat after meat degradation, as will be discussed in the following section.

3.2 | Degradation of fresh meat

Numerous previous studies [11, 31, 32] have investigated the changes in polarization-based properties of raw meat over time, highlighting the potential of Mueller matrix imaging in assessing meat freshness. Consistent with these findings, our research has revealed significant alterations in the polarimetric characteristics of meat tissues, most particularly in skeletal muscle. These modifications are wavelength-dependent, as we will demonstrate, with particular relevance observed in the red and NIR regions of the spectrum.

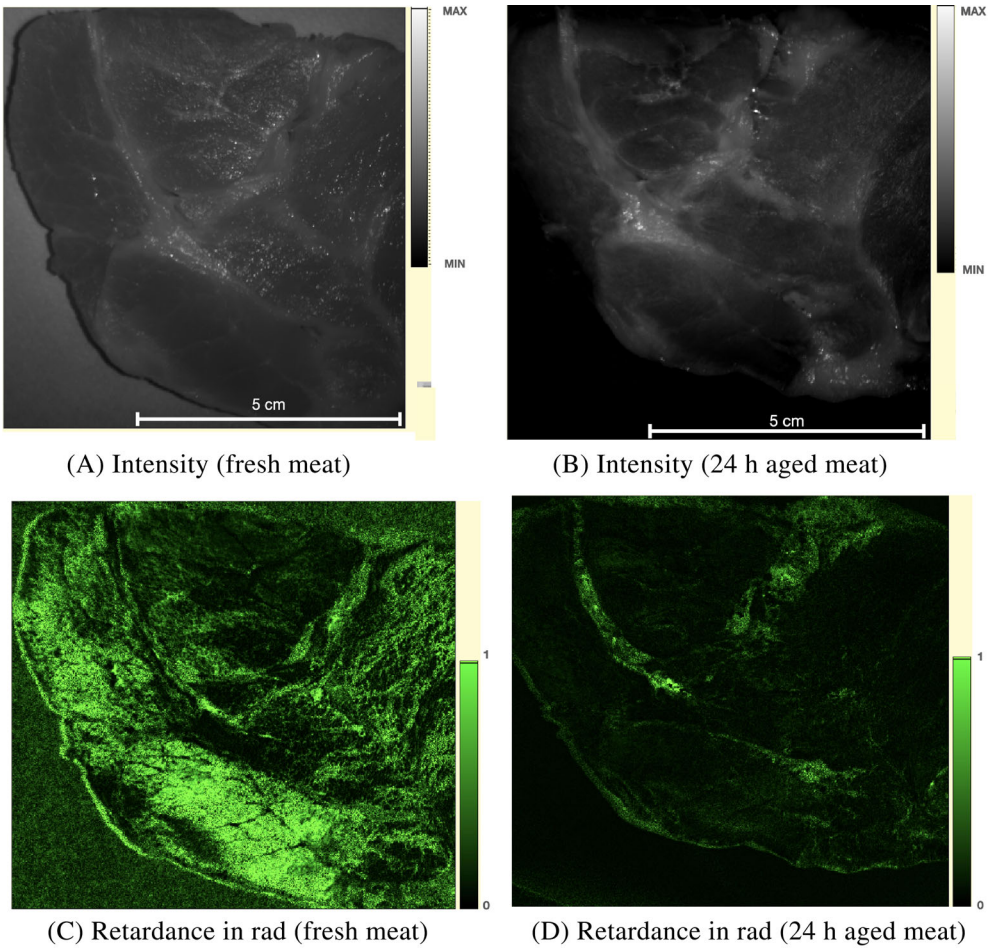

FIGURE 5 Compared intensity (A, B) and retardance (C, D) of a pork meat sample before and after aging for 24h. The measurement wavelength is 660 nm.

Figure 5 shows a comparison of intensity and retardance, measured at 660 nm, between the fresh meat sample (Figure 5A,C) and the same sample after 24 h, stored in air at room temperature (Figure 5B,D). The small shifts in the position of the sample from 1 day to the other happened because after storage it was manually repositioned in the MM imaging system. This was taken into account for our quantitative analysis. As in the previous sections, all the reported images have a resolution of 600×600 pixels which corresponds to an area of $8.5 \times 8.5\ \text{cm}^2$. A decrease in both the intensity of backscattered light and retardance can be seen. For the case of skeletal muscle and fat tissues, the results are quantified in the graphs shown in Figure 6.

For the fresh sample, intensity (I), diattenuation (D_m) and retardance (R_m) values for the skeletal muscle of $I = 289 \pm 37$ (arbitrary units), $D_m = 0.027 \pm 0.005$ rad and $R_m = 0.555 \pm 0.164$ rad have been obtained, while for the 24-h aged sample, the values changed to $I = 235 \pm 35$ (arbitrary units), $D_m = 0.017 \pm 0.005$ rad and $R_m = 0.055 \pm 0.027$ rad. Notably, the retardation of the skeletal muscle diminished in a $\sim 90\%$ in a time-lapse of 24 h, and a very similar trend was also seen for the diattenuation. At the same time, Figure 6 shows that the DI increased with the meat aging, indicating a reduction in the overall amount of multiple scattering. These are the most remarkable changes we observed during the meat degradation process. However, it is worth noting that this particular behavior has not been documented in previous studies and seems to contradict the findings reported in [31], where an increase in retardation values over time was attributed to muscle fiber densification resulting from water loss.

In our opinion, the observed reduction in retardation and diattenuation can be attributed to variations in the composition and structure of skeletal muscle over time. One of the primary components of muscle is water, which is lost during storage at room temperature. Additionally, muscle contains fibrillar proteins, which undergo oxidation processes and pH changes upon exposure to air, resulting in enzymatic degradation that changes their structure and composition. We think that changes ultimately lead to decreased tension or shrinkage in muscle fibers, explaining the observed diminution in total diattenuation and retardation shown in

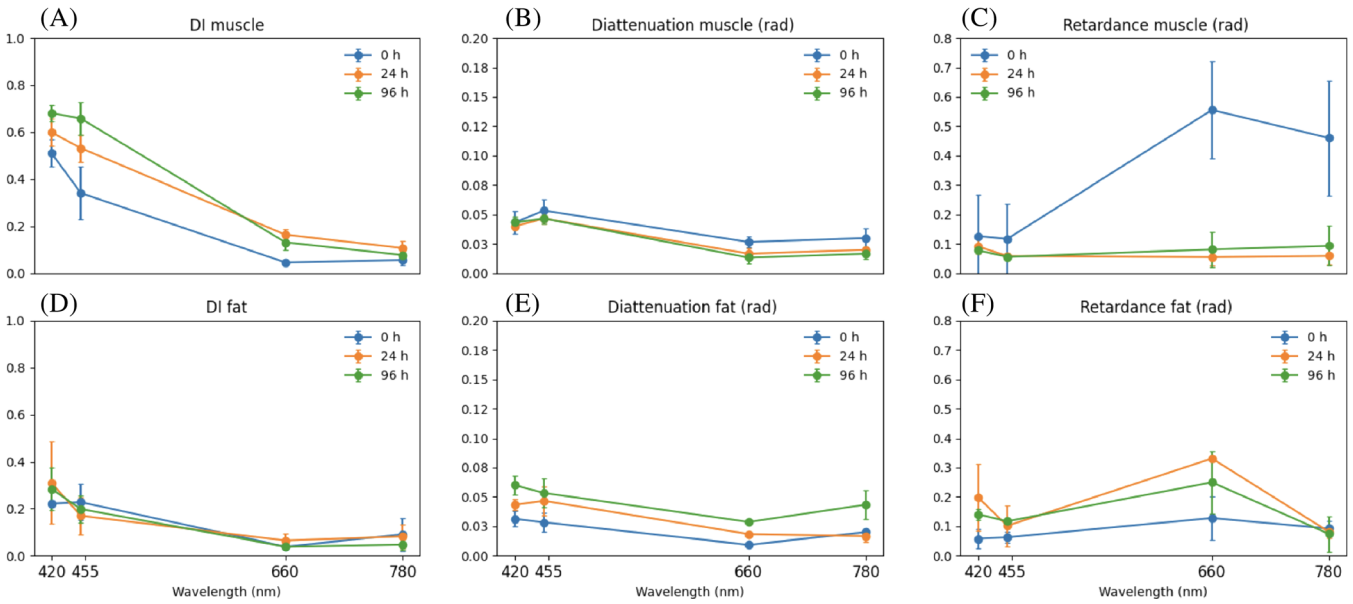

FIGURE 6 Variation over time of the DI, diattenuation and retardance as a function of wavelength for muscle (A–C) and fat (D–F) tissues of the pork meat sample.

Figures 5 and 6. These effects could be also responsible for the increase in meat tenderness over time.

We did not detect any substantial change in the connective tissues over time which suggests that the extracellular matrix of connective tissue did not suffer any significant degradation. However, the case of fat was different since we observed a change in diattenuation and retardance values at 660 nm. They increased from $D_m = 0.009 \pm 0.001$ rad and $R_m = 0.127 \pm 0.073$ rad for the fresh sample to $D_m = 0.018 \pm 0.002$ rad and $R_m = 0.331 \pm 0.008$ rad for the 24 h aged one (Figure 6). Fats are made up of triglycerides, which, when in contact with air for some time oxidize, leading to structural and chemical changes that in this case seem to result in a slightly less isotropic optical response and therefore in their ability to alter the polarization of the incident light, thus causing an increase in retardance and diattenuation values. The ultimate physiological reason for these changes is at present, unclear to us, but likely can be attributed to the formation of certain crystals or aggregates in oxidized fat that are absent in fresh meat.

Similar results were observed in the same meat sample when the measurements were repeated after 72 h of refrigeration (following an initial 24h period at room temperature). Figure 6 illustrates that there were no substantial variations observed between the measurements taken at 24 and 96 h. This suggests that the majority of changes in the meat, which polarimetry is capable of detecting, occur early on in the degradation process.

4 | CONCLUSIONS

In conclusion, this study provides a comprehensive investigation into the application of wide-field Mueller matrix polarimetry on essential biological tissues, including muscle, fat, connective tissue, and skin. Through spectral analysis, a comparison of their polarimetric properties has been presented. The results demonstrate a decrease in the DI with increasing wavelength, indicating the impact of penetration depth and the number of scattering events on the polarization of detected light. Notably, the reddish part of the spectrum shows very low but relatively stable DI values, only with a slight increase observed in fat tissue in the NIR. This trend can be attributed to the longer penetration depth of longer wavelengths, leading to more scattering events and reduced polarization of the detected light.

Furthermore, for muscle tissue, the low absorption of myoglobin in the red and NIR ranges leads to a notable increase in retardance values compared to measurements in the blue part of the spectrum that we attribute to the increased path of photons through fibrous tissue. Connective tissue, characterized by organized collagen fibers generally exhibits the highest diattenuation and retardance values among the analyzed tissues. In contrast, tissues lacking the same level of organization, such as fat, demonstrate much lower diattenuation and retardance values.

Our research has also revealed significant alterations in the polarimetric characteristics of meat tissues over time. Most important changes were observed in skeletal

muscle tissues, especially for wavelengths corresponding to the red and NIR spectrum. Within a 24-h period, we observed a very significant decrease of diattenuation and retardance values exhibited by skeletal muscle tissues compared to their "fresh" counterparts, whereas for fat tissues there was some increase in these optical effects. These changes in optical properties can be attributed to variations in the composition, structure, and oxidation processes taking place within the muscle and fat tissues.

ACKNOWLEDGMENTS

This work was supported by Ministerio de Ciencia Innovación y Universidades RYC2018-024997-I, TED2021-129639B-I00, PID2022-138699OB-I00, and PDC2022-133625-I00 (MCIU/AEI/FEDER, UE).

CONFLICT OF INTEREST STATEMENT

The authors declare no conflicts of interest.

DATA AVAILABILITY STATEMENT

The data that support the findings of this study are available from the corresponding author upon reasonable request.

ORCID

Oriol Arteaga https://orcid.org/0000-0001-9015-0237

REFERENCES

[1] J. L. Pezzaniti, R. A. Chipman, *Opt. Eng.* **1995**, *34*, 1558.
[2] R. A. Chipman, E. A. Sornsin, J. L. Pezzaniti, *International Symposium on Polarization Analysis and Applications to Device Technology*, Vol. 2873, SPIE, Yokohama **1996**, p. 5.
[3] N. Ghosh, I. A. Vitkin, *J. Biomed. Opt.* **2011**, *16*, 110801.
[4] A. Baldwin, J. Chung, J. Baba, C. Spiegelman, M. Amoss, L. Coté, *Proceedings of the 25th Annual International Conference of the IEEE Engineering in Medicine and Biology Society (IEEE Cat. No. 03CH37439)*, Vol. 2, IEEE, Cancun **2003**, p. 1027.
[5] M.-R. Antonelli, A. Pierangelo, T. Novikova, P. Validire, A. Benali, B. Gayet, A. de Martino, *Opt. Express* **2010**, *18*, 10200.
[6] P. G. Ellingsen, M. B. Lilledahl, L. M. S. Aas, C. L. Davies, M. Kildemo, *J. Biomed. Opt.* **2011**, *16*, 116002.
[7] H. He, M. Sun, N. Zeng, E. du, S. Liu, Y. Guo, J. Wu, Y. He, H. Ma, *J. Biomed. Opt.* **2014**, *19*, 106007.
[8] E. Du, H. He, N. Zeng, M. Sun, Y. Guo, J. Wu, S. Liu, H. Ma, *J. Biomed. Opt.* **2014**, *19*, 076013.
[9] Y. Wang, H. He, J. Chang, N. Zeng, S. Liu, M. Li, H. Ma, *Micron* **2015**, *79*, 8.
[10] T. Novikova, J. Rehbinder, S. Deby, H. Haddad, J. Vizet, A. Pierangelo, P. Validire, A. Benali, B. Gayet, B. Teig, A. Nazac, B. Drévillon, F. Moreau, A. De Martino, *Clinical and Translational Biophotonics, TTh3B–2*, Optical Society of America, Fort Lauderdale, FL **2016**.
[11] H. He, C. He, J. Chang, D. Lv, J. Wu, C. Duan, Q. Zhou, N. Zeng, Y. He, H. Ma, *J. Biophotonics* **2017**, *10*, 664.
[12] J. Chue-Sang, Y. Bai, S. Stoff, M. Gonzalez, N. Holness, J. Gomes, R. Jung, A. Gandjbakhche, V. V. Chernomordik, J. C. Ramella-Roman, *J. Biomed. Opt.* **2017**, *22*, 086010.
[13] Y. Dong, S. Liu, Y. Shen, H. He, H. Ma, *Biomed. Opt. Express* **2020**, *11*, 4960.
[14] H. R. Lee, I. Saytashev, V. N. Du Le, M. Mahendroo, J. Ramella-Roman, T. Novikova, *Sci. Rep.* **2021**, *11*, 1.
[15] A. Le Gratiet, A. Mohebi, F. Callegari, P. Bianchini, A. Diaspro, *Appl. Sci.* **2021**, *11*, 1632.
[16] H.-M. Le, T. H. Le, Q. H. Phan, T. T. H. Pham, *Opt. Commun.* **2022**, *502*, 127420.
[17] J. Rehbinder, J. Vizet, J. Park, R. Ossikovski, J. C. Vanel, A. Nazac, A. Pierangelo, *Sci. Rep.* **2022**, *12*, 1.
[18] R. A. Chipman, *Handbook of Optics*, Ch. 15, 3rd ed., OSA, New York **2009**.
[19] D. Sabatke, M. Descour, E. Dereniak, W. Sweatt, S. Kemme, G. Phipps, *Opt. Lett.* **2000**, *25*, 802.
[20] O. Arteaga, J. Freudenthal, B. Wang, B. Kahr, *Appl. Opt.* **2012**, *51*, 6805.
[21] D. Gottlieb, O. Arteaga, *Opt. Lett.* **2021**, *46*, 3139.
[22] O. Arteaga, S. Bian, *Optical Polarimetric Modalities for Biomedical Research*, Ch. 4, Springer, Cham **2023**.
[23] D. Gottlieb, S. Aguado, J. Gomis-Brescó, A. canillas, E. Pascual, O. Arteaga, *Polarized Light and Optical Angular Momentum for Biomedical Diagnostics 2022*, Vol. 11963, SPIE, San Francisco, CA **2022**, p. 54.
[24] N. Ghosh, M. F. Wood, I. A. Vitkin, *Opt. Commun.* **2010**, *283*, 1200.
[25] R. Ossikovski, *Opt. Lett.* **2011**, *36*, 2330.
[26] R. Ossikovski, *Opt. Lett.* **2012**, *37*, 220.
[27] O. Arteaga, *J. Opt. Soc. Am. A* **2017**, *34*, 410.
[28] R. Ossikovski, O. Arteaga, *Opt. Lett.* **2014**, *39*, 4470.
[29] O. Arteaga, R. Ossikovski, *Polarized Light in Biomedical Imaging and Sensing*, Ch. 5, Springer, Cham **2023**.
[30] J. J. Gil, E. Bernabeu, *Opt. Acta* **1986**, *33*, 185.
[31] M. Peyvasteh, A. Popov, A. Bykov, A. Pierangelo, T. Novikova, I. Meglinski, *J. Biophotonics* **2021**, *14*, e202000376.
[32] A. Blokhina, M. Kleshchenok, I. Nekrylov, S. Mednikov, V. Ryzhova, I. Konyakhin, *Tenth International Symposium on Precision Engineering Measurements and Instrumentation*, Vol. 11053, SPIE, Kunming **2019**, p. 1139.

How to cite this article: I. Pardo, S. Bian, J. Gomis-Brescó, E. Pascual, A. Canillas, S. Bosch, O. Arteaga, *J. Biophotonics* **2023**, e202300252. https://doi.org/10.1002/jbio.202300252